Spatiotemporal Monte Carlo transport methods in x-ray semiconductor detectors: Application to pulse-height spectroscopy in a-Se

Yuan Fang[a)]
*Division of Imaging and Applied Mathematics, Office of Science and Engineering Laboratories,
Center for Devices and Radiological Health, U.S. Food and Drug Administration,
10903 New Hampshire Avenue, Silver Spring, Maryland 20993-0002 and Department of Electrical
and Computer Engineering, University of Waterloo, Waterloo, Ontario N2L3G1, Canada*

Andreu Badal
*Division of Imaging and Applied Mathematics, Office of Science and Engineering Laboratories,
Center for Devices and Radiological Health, U.S. Food and Drug Administration,
10903 New Hampshire Avenue, Silver Spring, Maryland 20993-0002*

Nicholas Allec and Karim S. Karim
*Department of Electrical and Computer Engineering, University of Waterloo, Waterloo,
Ontario N2L3G1, Canada*

Aldo Badano
*Division of Imaging and Applied Mathematics, Office of Science and Engineering Laboratories,
Center for Devices and Radiological Health, U.S. Food and Drug Administration,
10903 New Hampshire Avenue, Silver Spring, Maryland 20993-0002*

Purpose: The authors describe a detailed Monte Carlo (MC) method for the coupled transport of
ionizing particles and charge carriers in amorphous selenium (a-Se) semiconductor x-ray detectors,
and model the effect of statistical variations on the detected signal.
Methods: A detailed transport code was developed for modeling the signal formation process in
semiconductor x-ray detectors. The charge transport routines include three-dimensional spatial and
temporal models of electron-hole pair transport taking into account recombination and trapping.
Many electron-hole pairs are created simultaneously in bursts from energy deposition events.
Carrier transport processes include drift due to external field and Coulombic interactions, and diffu-
sion due to Brownian motion.
Results: Pulse-height spectra (PHS) have been simulated with different transport conditions for a
range of monoenergetic incident x-ray energies and mammography radiation beam qualities. Two
methods for calculating Swank factors from simulated PHS are shown, one using the entire PHS
distribution, and the other using the photopeak. The latter ignores contributions from Compton scat-
tering and K-fluorescence. Comparisons differ by approximately 2% between experimental meas-
urements and simulations.
Conclusions: The a-Se x-ray detector PHS responses simulated in this work include three-
dimensional spatial and temporal transport of electron-hole pairs. These PHS were used to calculate
the Swank factor and compare it with experimental measurements. The Swank factor was shown to
be a function of x-ray energy and applied electric field. Trapping and recombination models are
all shown to affect the Swank factor. © *2012 American Association of Physicists in Medicine.*
[DOI: 10.1118/1.3669486]

Key words: Swank factor, semiconductor detector, Monte Carlo, amorphous selenium

I. INTRODUCTION

X-ray detectors are important components of medical imag-
ing, dosimetry, spectroscopy, security, and industrial imag-
ing systems. Semiconductor detectors are advantageous for
these applications because of their good energy resolution,
high efficiency, and high carrier yield per incident x-ray.[1]
Semiconductor detectors employ photoconductive materials
such as silicon, germanium, and amorphous selenium to con-
vert x-rays directly into electric signal. In medical imaging
applications, semiconductor detectors are used in a wide

range of modalities including full-field digital mammog-
raphy (FFDM) and computed tomography (CT).[2,3] Semicon-
ductor materials such as stabilized a-Se and other high-Z
materials have recently emerged as candidates for new imag-
ing technologies including breast tomosynthesis and photon-
counting mammography.[4,5]

A critical performance parameter of x-ray imaging detec-
tors is the statistical variation in the detected signal per pri-
mary quanta, known as Swank factor or information factor.[6]
These statistical fluctuations are due to random events such
as Compton scattering, K-fluorescence, photoelectric and

Compton electron range, and transport of electron-hole pairs. Electron-hole pairs are the fundamental information carriers created along the path of the charged particle (primary radiation or secondary particle) through the detector. Transport of electron-hole pairs is especially significant in a-Se detectors due to low carrier mobility. In order to increase the detector sensitivity, high electric fields are typically used to cause carriers to drift toward the electrodes, reducing recombination and trapping of electrons and holes.

Experimentally, pulse-height spectroscopy measurements have been used to determine Swank factor in a-Se detectors.[7,8] In a typical experimental setup, the a-Se sample is placed in an aluminum box to reduce noise, and exposed to monoenergetic x-ray photons from radioisotopes or by filtering an x-ray tube spectrum with an appropriate combination of filter materials. Long amplifier shaping times of up to 64 μs have been used to accommodate for the low electron mobility in a-Se. However, measured spectra are noisy due to energy dispersion of x-ray sources, additional noise introduced by the high-voltage source, long signal shaping times, and read-out electronics. Gaussian fitting of the spectral peak to determine the distribution's mean and variance also ignores lower energy events such as those from Compton scattering (also known as the Compton continuum), fluorescent escape, and reabsorption which contribute to the pulse-height spectra.

Modeling of semiconductor detectors can provide insight into the fundamental limitations and optimization strategies of the imaging system. Among modeling methods, Monte Carlo (MC) techniques have proven effective at studying spatial and energy resolution and Swank factor in scintillator detectors.[9,10] A number of available MC simulators exist for modeling radiation transport of photons, electrons, and positrons: PENELOPE (Ref. [11]) and EGSNRC.[12] Other simulators include models for heavy charged particles and neutrons: MCNP,[13] GEANT4,[14] and FLUKA.[15] These MC simulators have been validated with established databases and offer accurate models for the simulation of various particle interactions. In addition, the use of advanced geometry packages has allowed for simulation of complicated detector or anatomical structures.[16] However, one limitation of available general purpose MC simulators is the lack of ability to create and transport electron-hole pairs for the modeling of semiconductor detectors.

In the past, some custom MC simulators have been developed for one-dimensional spatial transport studies of electron-hole pair interactions such as trapping and recombination and their effects on sensitivity and density of states in a-Se detectors.[17,18] These models provide flexibility in the implementation of complex recombination and trapping models but ignore the charge spreading due to high energy electron interactions, and the lateral spreading during electron-hole pair transport due to diffusion processes. To include recombination and diffusion processes during transport, Fourkal *et al.*[19] studied the three-dimensional transport of electron-hole pairs by extending EGSNRC with custom transport routines. However, due to computing limitations, only the detection statistics of a single charge carrier (hole)

per primary history were simulated in the nanometer range. This model is not useful for generating the detector pulse-height response and also ignores trapping. Thus, not useful for Swank factor studies.

Beside MC methods, analytical models have been used alone or in combination with MC methods for simulation of imaging detectors.[20] Compared to MC methods, analytical methods do not require long computation times and are efficient at solving problems with simple geometries and electric field distributions that can be mathematically represented. However, limitations arise when modeling three-dimensional carrier transport in complex geometries, nonlinear field distributions and when taking into account the stochastic events that affect radiation transport including trapping and recombination.

Beside MC methods and analytical models, numerical techniques such as the finite element methods (FEM) are tools utilized for the simulation of transport process in a wide range of semiconductor devices.[21–23] FEM tools offer many advantages such as implementation of complicated geometries, detailed visualization, and the ability to adjust precision in target areas. FEM and MC methods can be combined[24] or used in conjunction[25] to model carrier transport problems in a variety of media. These works allow for the flexibility of combining less computationally consuming FEM methods with stochastic models of MC methods. However, some challenges include modeling the system with numerically stable equations, choosing the appropriate boundary conditions to obtain meaningful results and the stochastic models necessary for modeling radiation absorption and transport in semiconductor materials.

In this paper, we report on a novel detailed transport code for modeling the signal formation process in semiconductor x-ray detectors. Compared to previous work available that study the transport characteristics of electron-hole pairs[17,18] and detection statistics of a single charge carrier per primary photon,[19] this code includes three-dimensional spatial and temporal transport of electron-hole pairs and allows for simulation of detector pulse-height spectra (PHS) responses. The full PHS distribution can be used to estimate the Swank factor of an x-ray detector. In addition, our transport code allows for tracking energetic electrons as well as electron-hole pairs in the presence of a continuous applied electric field. Using this transport code, we simulated the PHS of an a-Se detector for a range of incident x-ray photon energies with varying applied electric field and carrier models taking into account recombination and trapping. The simulated PHS are used for calculating the Swank factor as a function of incident-photon energy and compared with experimental data provided from previously reported PHS measurements.[7]

II. METHODS

II.A. Theory

Electron-hole pairs are created by ionizing radiation from energy deposition events. Important parameters to be considered for the creation of electron-hole pairs include: energy deposition in the initial interaction, ionization energy of the

detector material, initial carrier separation, and burst characteristics. The implementation of drift and diffusion under Coulombic attraction and external applied fields and trapping is discussed in detail in Sec. II B.

II.A.1. Energy deposition

X rays interact with the atoms of the semiconductor material through various mechanisms. For an incident photon in the energy range of medical imaging applications, the main mechanisms are: Rayleigh scattering, Compton scattering, and photoelectric absorption. The interaction cross-sections are a function of the energy and the material. The dominant photon interaction mechanism in the diagnostic energy range is photoelectric absorption, which creates a secondary electron with most of the energy of the initial x-ray and therefore capable of producing many electron-hole pairs. As the high energy secondary electron travels through the detector material, it gradually loses energy through inelastic scattering and the energy lost, E_d, is deposited in the semiconductor material.

II.A.2. Ionization energy

The energy deposited in the semiconductor can lead to either phonon emission or ionization. Thus, determining the exact number of electron-hole pairs created, N_{EHP}, is not trivial. As a first-order approximation, the mean number of pairs created, $\overline{N}_{EHP}$, can be approximated with the mean energy expended to create one pair, W_0, by

$$\overline{N}_{EHP} = E_d/W_0. \tag{1}$$

In turn, W_0 can be approximated by the semiempirical formula developed by Que and Rowlands[26]

$$W_0 \approx 2.2 E_{gap} + r h v_p, \tag{2}$$

where E_{gap} is the band gap of amorphous selenium, $h v_p$ is the phonon energy, and r is a uniform random number between 0 and 1. This approximation, taking into account the phonon emission and electron-hole pair creation components, is valid for a range of amorphous materials and phonon energies.

II.A.3. Initial carrier separation

When an electron-hole pair is created, it has been postulated[27] that the electron and the hole lose their initial kinetic energy in a thermalization process, after which they are separated by a finite distance r_0. This distance can be estimated for a given initial kinetic energy of the pair, hv, and applied electric field, E_{app} using the Knight–Davis equation,[27] where D is the diffusion constant, ε is the dielectric constant, and e is the elementary charge

$$\frac{r_0^2}{D} = \frac{(hv - E_{gap}) + \dfrac{e^2}{4\pi\varepsilon r_0} + e E_{app} r_0}{h v_p^2}. \tag{3}$$

This theory was originally developed for electron-hole pair creation in semiconductor materials from low energy optical photons that lead to only one electron-hole pair per quantum.

In the case of a high energy x-ray photon, many electron-hole pairs are created, and thus validity of the model is difficult to determine. For instance, due to the high concentration of carriers, not only is the electron and hole separation distance per pair important but also the relative distance between pairs can greatly affect carrier transport such as recombination in the electron-hole pair history. The separation distance, r_0, is calculated using the Knight–Davis equation. This equation was solved by finding the cubic roots, yielding one positive root and two imaginary roots. Only the positive root is used as a separation distance. Both types of carriers diffuse during the initial separation process. Since hole mobility is much greater than the electron mobility, the hole diffusion coefficient is used in the Knight-Davis equation.

II.A.4. Burst

The concept of a burst is defined as the cloud (spatio-temporal distribution) of electrons and holes generated after a local deposition of energy given an assumed thermalization distance indicated by r_0.[28] Energy transferred in electron inelastic collisions with outer-shell electrons can lead to excitation of plasma waves and create multiple electron-hole pairs. These pairs constitute a burst, and the burst size is dependent on the energy of the incident particle and the material plasma frequency. According to the Bohr adiabatic criterion,[29] the burst size, r_b, can be approximated using the following expression:

$$r_b \approx \frac{v}{\omega_{pe}}, \tag{4}$$

where v is the velocity of the incident particle and ω_{pe} is a material parameter known as the plasma frequency. The plasma frequency is dependent on the material electron mass and density. The concept of a burst is introduced in conjunction to the thermalization of carriers, in order to provide a three-dimensional distribution model for electron-hole pair creation.

In this work, the size of the burst is modeled with a spherical radius, as a function of the interaction electron velocity, shown in Eq. (4). Diffusion of carriers is taken into account using the Knight–Davis model [Eq. (3)] when calculating the electron-hole pair separation distance and do not affect the size of the burst. The shape of the burst can be affected by the direction of the interacting electron. However, since the direction of the interaction electron and electron-hole pairs is constantly changing during the random walk in the detector material, a spherical burst model serves in principle as an acceptable initial assumption for this work.

II.A.5. Trapping

Many trapping effects have been modeled previously in one-dimension (z-direction) for a-Se detectors.[17] These include deep trap, shallow trap, trap releasing, trap filling, and trap center generation due to incident x-rays. Deep and shallow trapping differs in the trapping time of carriers. Deep traps have long trapping times on the order of seconds to minutes, while shallow traps may release carriers in fractions
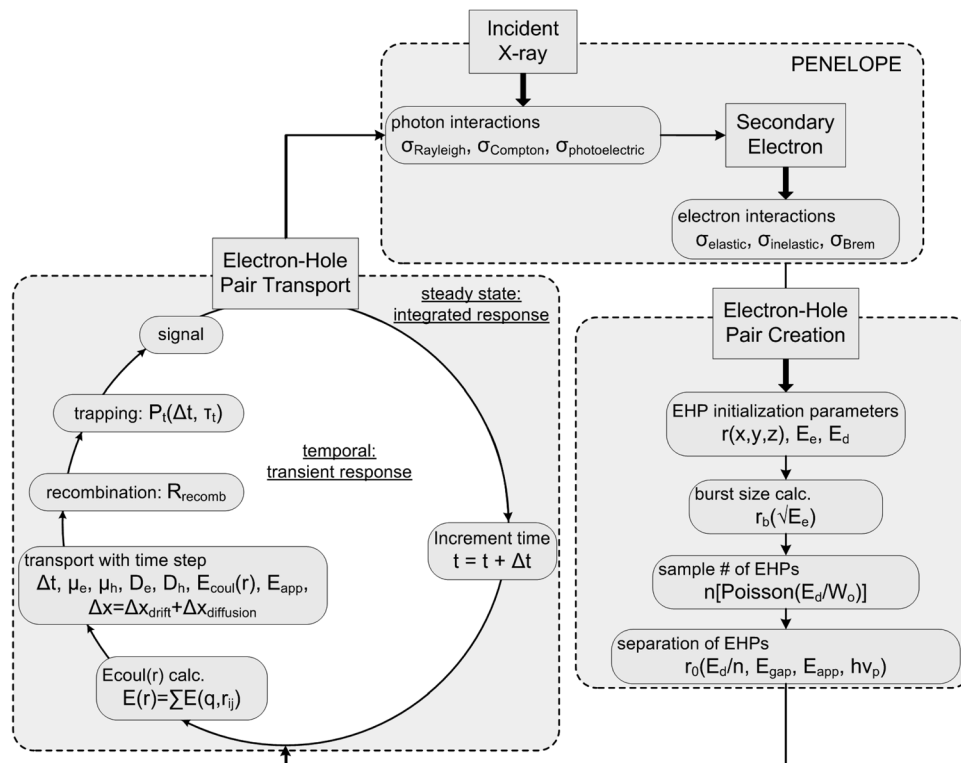
Fig. 1. Flow chart for the simulation of the signal formation process in semiconductor x-ray detectors. Simulation of photon and secondary electron with PENELOPE is coupled with novel transport code for detailed spatiotemporal simulation of electron-hole pairs.

of a microsecond or less. For simulation purposes, when a carrier is trapped in a deep trap, it is considered lost. However, when a carrier is trapped in a shallow trap, the release of this trapped carrier (perhaps in subsequent exposures) can contribute to the detected signal as well. As electron-hole pairs start to move in the material and get trapped, the number of available traps decreases as a function of time, x-ray exposure and carrier concentration. At the same time, a competing process of trap center creation is occurring due to x-ray bombardment of the semiconductor material.

II.B. Implementation

A custom Monte Carlo transport code, ARTEMIS (pArticle transport, Recombination, and Trapping in sEMconductor Imaging Simulations), has been developed for the purpose of simulation of electron-hole-pair transport. Various functions are implemented to model the physics outlined in Secs. II A and II B. The flow diagram for the implemented simulation framework is shown in Fig. 1. X-ray photon and secondary electron interactions in the presence of an external electric field are modeled by PENELOPE,[11] and the locations of inelastic electron interactions with energy deposition are coupled with the transport routines for electron-hole pair simulations. PENELOPE is written in FORTRAN, while the electron-hole pair transport code is written in C. The electron-hole pair transport source code is called as subroutines from the PENELOPE ionizing radiation transport code.

As shown in Fig. 1, the secondary electrons move in a random walk fashion and deposit energy at random locations in

the photoconductor. The electron-hole pairs generated in the bursts created from the deposition of energy are transported to the electrodes and may get trapped or recombine. All of these processes take place under an applied electric field. The creation of electron-hole pairs begins with three initialization parameters: interaction coordinates, $\vec{r}$, the energy of the interaction particle, E_e, and the amount of energy deposited, E_d. We postulate that when many electron-hole pairs are generated simultaneously, they are created as a distribution in a region instead of at a single interaction point. For this analysis, this region is considered to be a sphere and its radius given by the Bohr adiabatic criterion,[29] as a function of particle energy. Then, the number of electron-hole pairs generated is assumed to follow a Poisson distribution, with the mean calculated based on the ionization energy equation developed by Que and Rowlands.[26] As a first-order approximation, the energy deposited, E_d, is distributed equally among the electron-hole pairs assuming a constant ionization energy, W_0, of 5 eV calculated based on selenium band gap energy of 2.3 eV for simulation purposes. The ionization energy also contributes to the initial separation of the electron-hole pair and can be calculated using the Knight–Davis equation,[27] as a function of the material, amount of energy deposited and applied electric field. For a second order model, a distribution of ionization energy and burst radius could be used, to provide varying separation distances between pairs in the same burst region. The locations of the electron-hole pairs are initialized with an uniform distribution on the burst surface with separation distance, r_0. Currently, due to the large number of electron-hole pairs, each burst is simulated
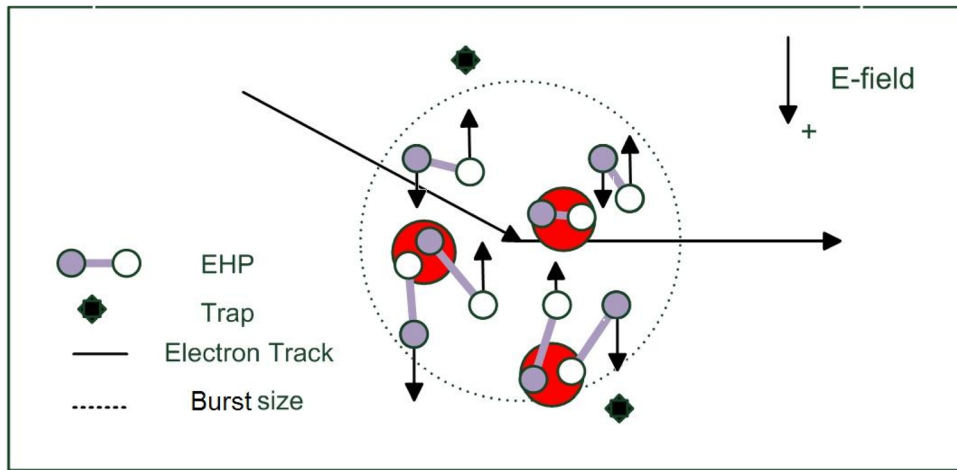
FIG. 2. Two-dimensional illustration of processes related to the creation and transport of electron-hole pairs. Recombination is represented with circles containing an electron and a hole.

separately for the transport including recombination and trapping considerations.

Once the electron-hole pairs are generated, the applied electric field pulls the holes and electrons to opposing electrodes. However, these charged carriers could be lost as they travel within the photoconductor as shown in Fig. 2 by two processes: recombination and trapping.[30]

Recombination can occur when an electron and a hole travel toward each other, and trapping can occur when an electron or hole reaches a lower energy state due to material impurities. In addition, carriers are subject to drift. The drift component takes into account applied electric field, E_{app}, and the Coulomb field due to other charge carriers. The resulting electric field for charge carrier i is given by

$$\vec{E}_i = \vec{E}_{app} + \sum_{j \neq i} \frac{1}{4\pi\varepsilon} \frac{q_j}{r_{ij}^2} \hat{r}_{ij}, \qquad (5)$$

where ε is the material dielectric constant, q is the elementary electric charge, r_{ij} is the separation distance between charge carrier i and j, and $\hat{r}_{ij}$ the direction vector. Once the electric field is known, the different components of displacement in a time step, Δt, can be found by

$$\Delta x_{dr} = \mu_i E_{x,i} \Delta t, \qquad (6)$$

where i denotes the current particle of interest, μ is its mobility, and E_x is the x component of the electric field. The components of the y and z directions can be found similarly. To find the diffusion components, the polar and azimuth angles are sampled from a uniform distribution, where the diffusion distance is given by $\sqrt{6D\Delta t}$.[32] Once the drift and diffusion component have been found, the total displacement in all directions can be found by adding the drift and diffusion components,

$$\Delta x = \Delta x_{dr} + \Delta x_{dif}. \qquad (7)$$

During transport, both drift and diffusion of carriers are calculated at each time step, where the drift component depends on the carrier mobility, electric field acting on the carrier and the simulation time step, and the diffusion component depends on the diffusion coefficient and the time step as shown in Eqs. (5)–(7).

The recombination of carriers is checked at each simulation step. Recombination occurs when an electron and a hole are sufficiently close together, making the Coulomb attraction so strong that they cannot escape each other. As carriers approach each other due to Coulomb attraction, their drift component from the Coulomb field increases as an inverse function of separation distance squared. Thus, as the separation distance is reduced, the simulation time step also should be reduced in order to accurately capture the movement of the carriers as they come close to each other. However, this comes at the expense of simulation time. To solve this problem, a recombination distance was used by Bartczak *et al.*[31] in their study of ion recombination in irradiated nonpolar liquids. In Bartczak's work, the recombination radius is a threshold used in the recombination model to stop simulations when a hole and an electron are found sufficiently close to each other. This parameter is needed because as oppositely charged carriers approach each other, their Coulomb attraction increases, and the distance between the electron and hole invariably decreases but never reaching zero, coupled with an increase in the probability of recombination. Therefore, each carrier's trajectory is tracked until they reach a critical recombination radius with an opposite charged carrier. At that point, recombination is assumed to occur. For electron-hole pair transport, typical electron-hole pair separation distances are in the range of 4–7 nm depending on the amount of energy deposited per pair. Since the carrier attraction due to Coulomb field is governed by Coulomb's law with inverse separation distance squared, at 1 nm separation, the magnitude of the attraction has been increased by at least 1 order of magnitude from the initial separation, thus much less likely to escape recombination. For simulation purposes, recombination radii of 0.5–1 nm have been tested, and the 1 nm case has been found to not hinder accuracy while improving simulation time.

The current implementation of trapping uses a simple model that only considers deep trapping. The probability of trapping, P_t, can be calculated as[17]

$$P_t = 1 - e^{-\frac{-\Delta t}{\tau_t}}, \tag{8}$$

where τ_t is the trapping time. Constant trapping times are used for electrons and holes, to give an estimate of the average carrier lifetime and the effect of applied electric field on carrier trapping probabilities in the semiconductor material. The probability of trapping is a function of time, and applied electric field affects the total carrier transit time from the interaction site to the appropriate electrode.

For this study, the a-Se detector is modeled as a 150 μm thick cylindrical slab with a 2.5 cm radius. The thickness is chosen to model a typical detector used in mammography, while the radius is chosen sufficiently large to approximate a large area detector. The electrode material, read-out electronics, and other components (e.g., substrate) are not considered in this study for simplicity. We used a pencil beam of monoenergetic x-rays as the source. Table I lists the parameters used in the Monte Carlo simulations. For all the results shown, at least 1 million primary x-ray photon histories have been simulated. The simulation time on average is approximately 20–30 min per photon energy and transport condition. The simulated Swank factor results have less than 1% variance.

Diagnostic energy ranges between 20 and 140 keV, with 20 keV steps and extra energies at 10, 12.5, and 13 keV near the K-edge have been simulated. Different transport models taking into account recombination only, or recombination and trapping were simulated with 4 and 30V/μm applied electric fields. For experimental comparison, we used 20V/μm applied bias consistent with the experiment setup.

The simulation code has been tested with a range of time steps, Δt, including 10^{-12}, 10^{-13}, 10^{-14}, and 10^{-15} s. The time step that gives the fastest simulation time without affecting the results was 10^{-13} s.

II.C. Calculation of Swank factor

The Swank factor,[33] also known as the information factor, has been derived from the following expression relating the detective quantum efficiency (DQE) at zero spatial frequency:

$$DQE(E) = \eta(E)I(E), \tag{9}$$

where η is the quantum efficiency (or interaction efficiency) of the detector as a function of thickness and energy. The Swank factor, I, is a statistical factor that arises from the fluctuations in the number of electron-hole pairs detected per absorbed x-ray. The Swank factor is defined as

TABLE I. Table of parameters used in the Monte Carlo simulations.

Simulation parameter (symbol)	Description	Value
μ_h	Hole mobility	1.9×10^{-1} cm^2/(Vs)
μ_e	Electron mobility	6.3×10^{-3} cm^2/(Vs)
D_h	Hole diffusion coefficient	4.9×10^{-3} cm^2/s
D_e	Electron diffusion coefficient	1.63×10^{-4} cm^2/s
ϵ_{Se}	Dielectric constant, Se	6.3

$$I = \frac{M_1^2}{M_0 M_2}, \tag{10}$$

where M_n is the nth moment of the electron-hole pair PHS distribution

$$M_n = \sum_x p(x)x^n, \tag{11}$$

and the fluctuations in x (number of detected electron-hole pairs) are given by the probability distribution, $p(x)$. Alternatively, the definitions of the mean and standard deviation of the distribution can be used to estimate I,

$$m = \frac{M_1}{M_0}, \quad \sigma^2 = \frac{M_2}{M_0} - \left(\frac{M_1}{M_0}\right)^2, \quad I = \frac{m^2}{m^2 + \sigma^2}. \tag{12}$$

When the detector response is a single photopeak, Swank factor depends only on the mean and variance of the Gaussian distribution of the photopeak

$$I = \frac{m_{photo-peak}^2}{m_{photo-peak}^2 + \sigma_{photo-peak}^2}. \tag{13}$$

However, this method for calculation of Swank factor is accurate only for estimating a single-peak spectrum in the PHS and cannot be used to model multiple spectral peaks in the PHS. Multiple spectral peaks are often observed in the PHS due to fluorescent x-rays escaping from the detector material and Compton scattering. Due to low spectral resolution and noise, the single Gaussian fitting method is used in Blevis' experimental measurements.[7] For the simulation results presented in this work, Swank factors have been calculated considering the full PHS distribution and with a single Gaussian fitting method to provide a comparison with experimental results.

III. RESULTS

III.A. Pulse-height spectrum

Figure 3 shows simulated pulse-height spectra using detailed spatiotemporal MC simulation, for electron-hole pair creation, transport with recombination only, and transport with recombination and trapping cases, and a range of monoenergetic incident energies.

The electron-hole pair creation case samples the number of electron-hole pairs created from energy deposition events without transport. This case represents the maximum (sensitivity or) number of electron-hole pairs created and could be potentially collected with perfect transport, i.e., without recombination and trapping. For the transport with recombination only case, many bursts of electron-hole pairs are created, initialized and transported. The transport takes into account carrier diffusion due to Brownian motion and drift due to the external applied electric field and Coulomb attraction/repulsion due to neighboring carriers. The probability of trapping is assumed to be zero for the recombination only case. For the transport with recombination and trapping case, both recombination and trapping of electron-hole pairs are taken into account for carriers moving in the detector. The x-axis shows the number of electron-hole pairs per kiloelectronvolt,

(a) 12.5 keV
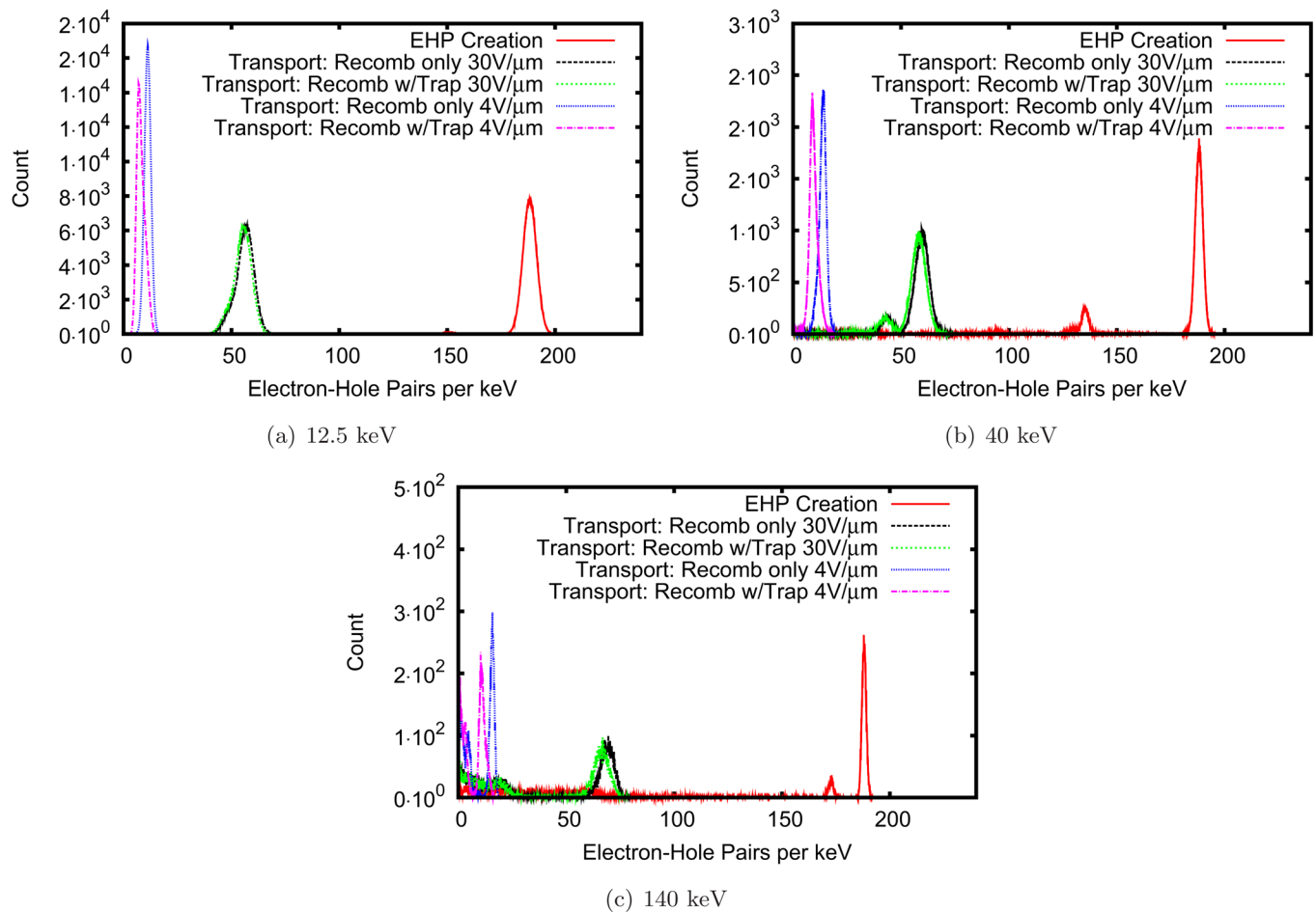

(b) 40 keV

(c) 140 keV

FIG. 3. Results of the detailed spatiotemporal Monte Carlo simulation. Plots of the pulse-height spectra, for no electron-hole pair transport, and transport with 4 and 30V/μm applied electric field with recombination only and with recombination and trapping for 12.5, 40, and 140 keV monoenergetic incident-photon energies.

i.e., normalized by the incident-photon energy. This allows for a realistic comparison between the PHS at different photon energies. The y axis is the number of electron-hole pairs collected per primary photon history. For accuracy, the bin size used is 10 electron-hole pairs per keV.

In Fig. 3(a), the incident-photon energy is 12.5 keV. There are five distinct spectral peaks corresponding to five different simulation cases: electron-hole pair creation, transport with recombination only at 30 and 4 V/μm, and transport with recombination and trapping at 30 and 4 V/μm. The highest spectral peak in the far right corresponds to the electron-hole pair creation case. The PHS consists of a single spectral peak because the incident-photon energy is below the K-edge of Se. In Fig. 3(b), the incident-photon energy is 40 keV, above the K-edge, and an additional lower spectral peak is observed due to generation and escape of fluorescent photons. In Fig. 3(c), the incident-photon energy is 140 keV, well above the K-edge, and significant lower energy counts are observed due to Compton scattering.

When the transport of electron-hole pairs is taken into account considering recombination, we observe that the spectral peak is significantly shifted to the left, because the number of electron-hole pairs detected is reduced due to recombination. The detection statistics also vary as a

function of applied electric field. For example, the PHS at 30V/μm versus 4 V/μm transport have different spectral peaks. At high-bias conditions, the carriers travel faster and thus more electron-hole pairs are detected.

When trapping is taken into consideration in conjunction with recombination, the effect of electric field becomes more
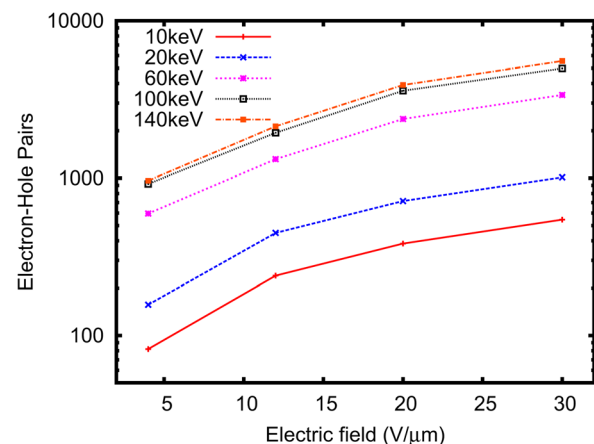

FIG. 4. Detected EHP as a function of incident-photon energy and applied electric field.
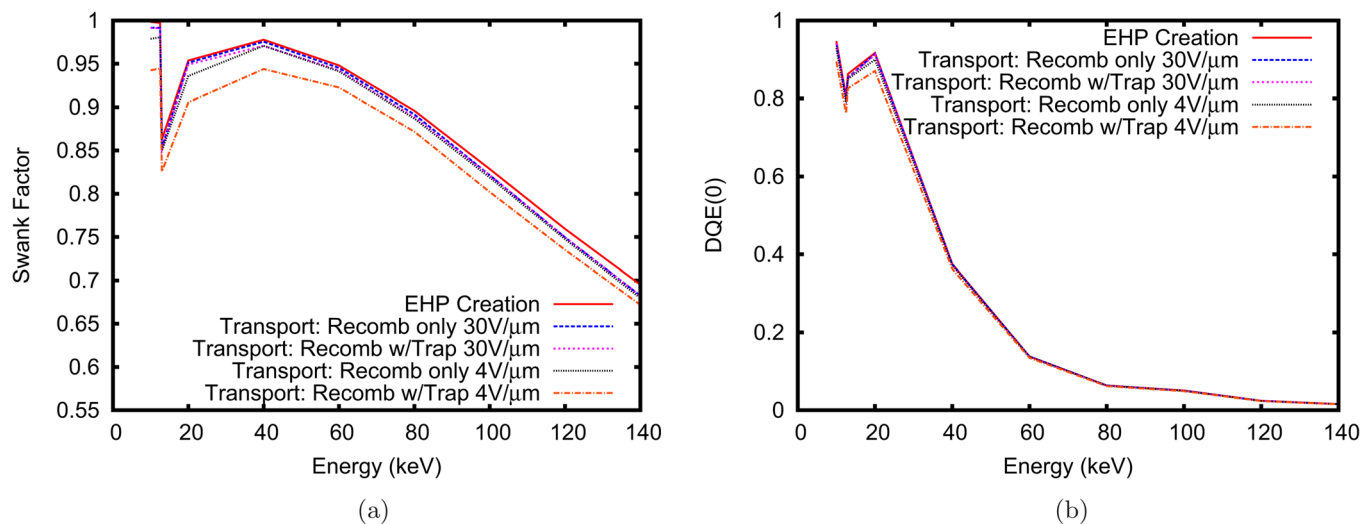
FIG. 5. (a) Simulated Swank factor as a function of incident-photon energy. (b) Simulated DQE at zero spatial frequency as a function of incident-photon energy.

apparent. For example, at low-bias conditions, for instance, 4 V/μm, the simulated PHS show a significant shift to the left. However, at high-bias conditions, for instance, 30 V/μm, the effect of trapping on the number of electron-hole pairs detected is small.

Figure 4 depicts the number of detected electron-hole pairs as a function of electric field and incident-photon energy taking into account recombination and trapping. As the electric field increases from 4 to 30 V/μm, the number of detected electron-hole pairs increases. The number of detected electron-hole pairs also increases if the incident-photon energy is increased, depositing more energy and leading to generation of a larger number of carriers.

III.B. Swank factor

Figure 5(a) shows the Swank factor calculated from the simulated PHS as a function of incident-photon energy. For the electron-hole pair creation case, the Swank factor is close to one at energies below the K-edge and drops sharply at energies slightly higher than the K-edge. The Swank factor slowly recovers as the photon energy increases, up to approximately 40 keV, where it starts to fall again due to an increase in Compton scattering events. The transport with recombination only, and with recombination and trapping cases show slightly reduced Swank factors due to transport, with similar trends. Significant degradation in the Swank factor is observed for the transport with recombination and trapping case at low field conditions (4 V/μm) due to low carrier mobility and trapping effects. Figure 5(b) shows the DQE at zero spatial frequency calculated from the simulated Swank factor and quantum efficiencies calculated from attenuation coefficient data (as a function of x-ray energy) taken from the PENELOPE databases.[11] The simulation results in Fig. 5 use the full distribution of output signal consistent with Eqs. (10) and (12). The simulated DQE at zero
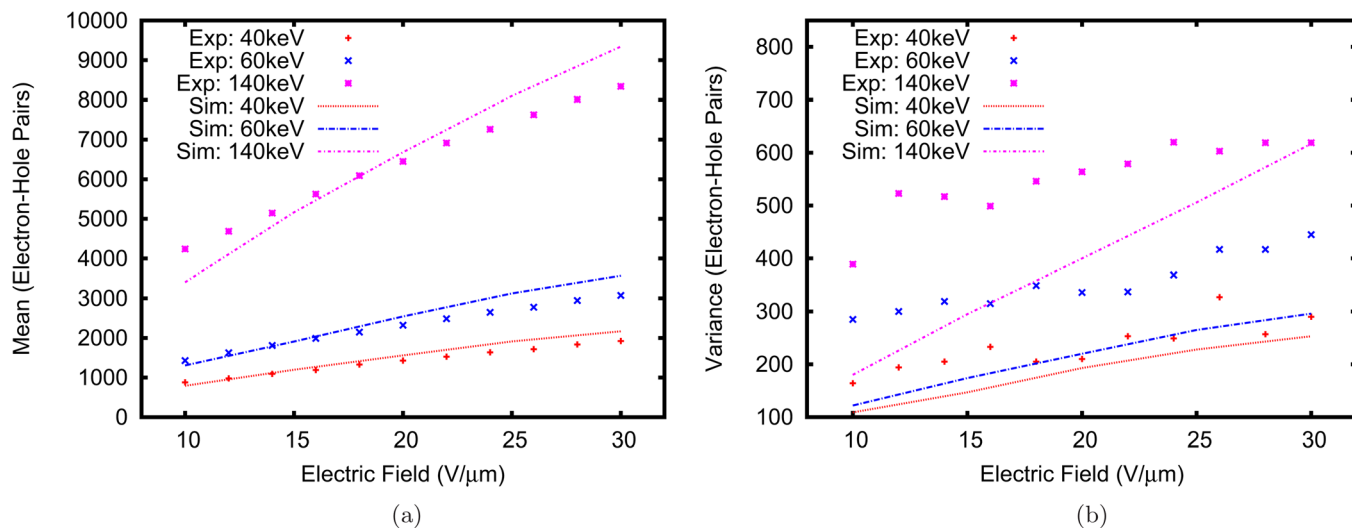

FIG. 6. (a) Comparison of simulated and experimental PHS—Gaussian fitted mean of the highest spectral peak as a function of applied field. (b) Comparison of simulated and experimental PHS—Gaussian fitted variance of the highest spectral peak as a function of applied field.

frequency results takes into account the detailed transport of electron-hole pairs, which results in lower Swank factor and DQE.

Figure 6 shows the Gaussian fit parameters used in Eq. (13) for simulated and experimental[7] PHS at 40, 60, and 140 keV as a function of applied electric field. The PHS are analytically fitted considering only the highest spectral peak in the distribution, and the Gaussian mean and variance are calculated. This method ignores all other peaks at lower energies (due to K-fluorescence, Compton, and noise) and provides a very poor estimate of the PHS distribution. Figure 6(a) shows a comparison of the simulated and experimental mean of the PHS distribution as a function of applied field. As the field increases, the mean number of detected electron-hole pairs and its variance increases. The number of electron-hole pairs also increases as the incident-photon energy increases. The experimental data show higher variance compared to the simulated data. This difference could be attributed to the perfect monoenergetic sources used in simulations in comparison to radioisotopes and multiple filter combinations used to generate near monoenergetic x-ray input spectra in the experiments. In addition, electronic noise and read-out circuits introduce additional variance in the measurements.

The differences in the simulated and experimental Swank noise are depicted in Fig. 7(a); the simulated Swank factors are obtained using Eq. (13). The simulated and experimental Swank factors have approximately 2% difference. Simulated Swank factor in all cases is higher than their experimental counterparts because of lower variance compared to the experimental data. In the experimental setup, longer amplifier shaping times of up to 64 μs are used to accommodate for the low electron mobility in a-Se and additional noise sources due to external high-voltage and read-out electronics need to be taken into account. Similar trends are observed between simulated and
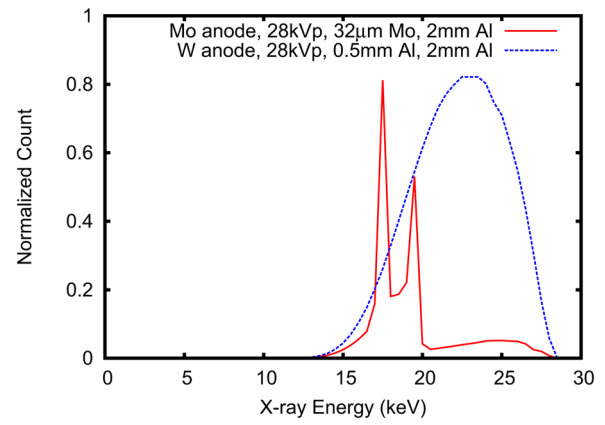

FIG. 8. Mammography beam qualities used in the Swank factor simulations: Mo/Mo (RQA-M 2) and W/Al from standard radiation quality (IEC 61267). Mo/Mo (RQA-M 2) is a molybdenum anode with 28 kVp tube voltage, 32 μm molybdenum filter and 2 mm Al filter. W/Al is a tungsten anode with 28 kVp tube voltage, 0.5 mm Al filter and 2 mm Al filter.

experimental Swank factors as the x-ray energy increase. Though not shown in the graph, this increasing trend of Swank factor as a function of electric field has been verified with simulations at 4 V/μm. Figure 7(b) shows a comparison of measured and simulated Swank factor as a function of incident x-ray energy. The plot shows an interesting comparison between Swank factors calculated from Gaussian fitting [using Eq. (13)] of the highest spectral peak versus taking into account the full PHS distribution using Eqs. (10) and (12). Significant differences in the Swank factor results are observed between the two methods. For instance, at 140 keV, the Gaussian fitted Swank is almost one, while the Swank factor taking into account the entire distribution is less than 0.7. Again, the Gaussian fitting method does not take into account Compton electrons, K-fluorescent photon generation and escape.
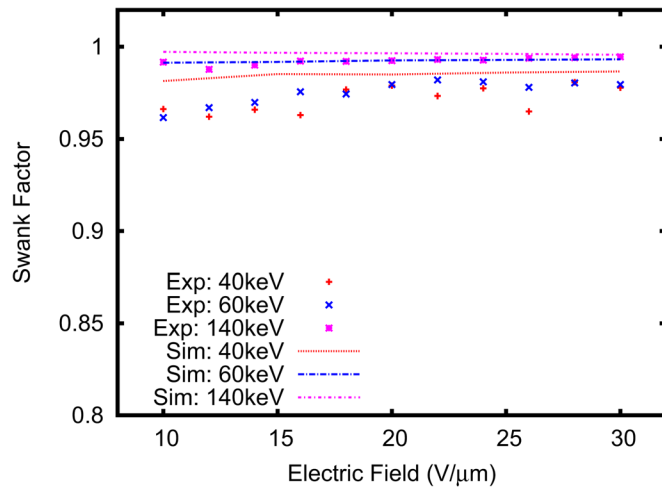
(a)
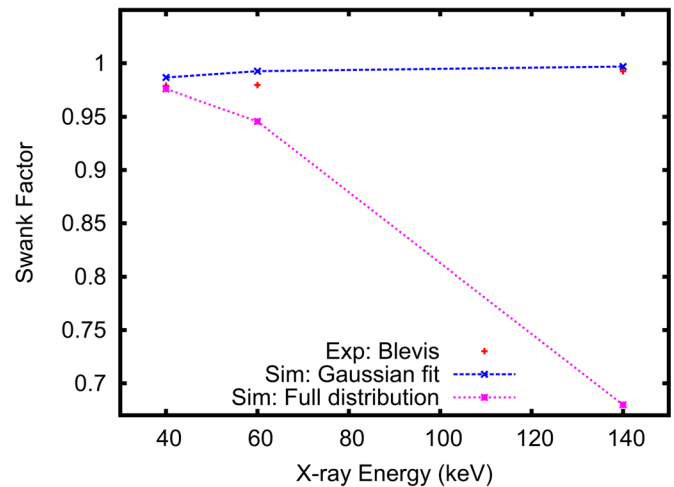
(b)

FIG. 7. (a) Comparison of measured and simulated Swank factor as a function of applied field. (b) Comparison of measured and simulated Swank factor as a function of incident-photon energy at 20 V/μm.
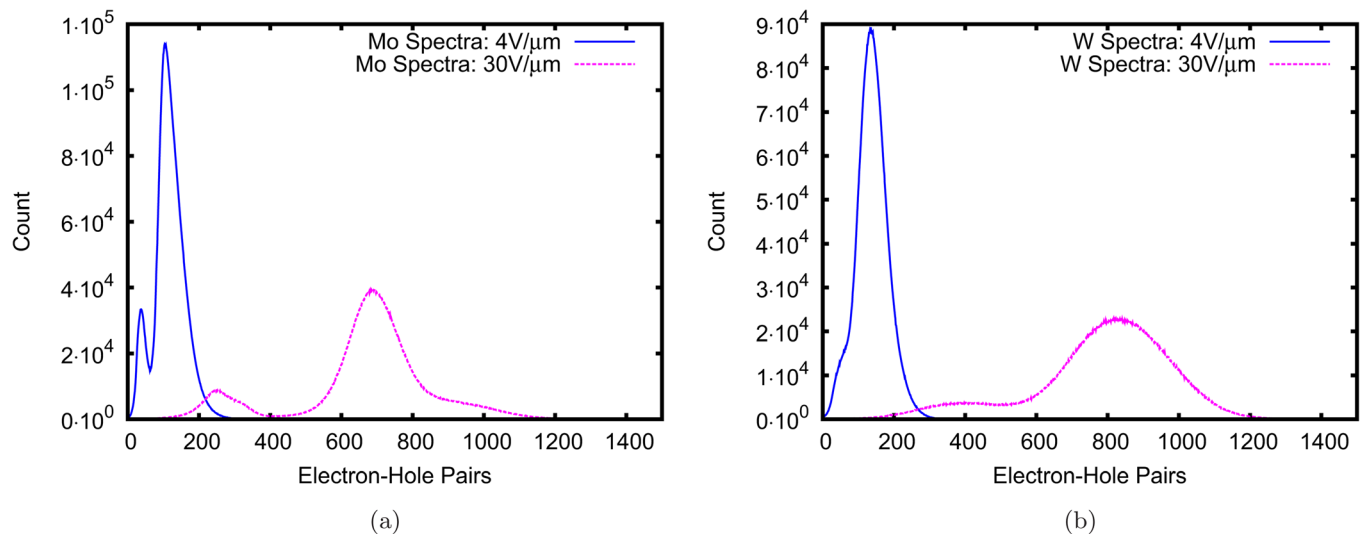
FIG. 9. (a) Simulated PHS with molybdenum mammography spectra as a function of electron-hole pair transport for 4 and 30V/μm applied electric field. (b) Simulated PHS with tungsten mammography spectra as a function of electron-hole pair transport for 4 and 30V/μm applied electric field.

Our code can simulate PHS not only for monoenergetic x-ray photons but also for x-ray spectra. The PHS for two known test mammography beam qualities have been simulated taking into account trapping and recombination effects. Figure 8 shows the energy spectrum of the two beam qualities used, generated with methods described by Boone *et al.*[34] Both beam qualities are taken from the standard radiation quality (IEC 61267), including tungsten and molybdenum anodes and tube voltage of 28 kVp. The molybdenum spectrum (RQA-M 2) includes a molybdenum filter of 32 μm and an additional 2 mm aluminum filter. The tungsten spectrum includes an aluminum filter of 0.5 mm and the same 2 mm aluminum filter.

The simulated PHS for both radiation qualities are shown in Fig. 9. The x-axis is in number of electron-hole pairs detected, and the two curves represent transport with 4 and 30 V/μm. Table II lists the simulated Swank factor for the molybdenum and tungsten spectra. Even though the molybdenum spectrum is more monoenergetic-like due to the two characteristic peaks, the corresponding Swank is worse. This is because the detector material properties, such as the K-edge energy where Swank degrades significantly due to fluorescent x-rays, need to also be taken into consideration. For a-Se, the K-edge energy is 12.6 keV, and monoenergetic x-ray simulations in Fig. 5 show that the Swank factor degrades significantly just above this energy and recovers slowly as the energy increases. From the normalized input spectrum in Fig. 8, the two characteristic peaks in the molybdenum spectrum are 17.5 and 19.5 keV, respectively, while

the tungsten spectrum is centered around 23.5 keV. So even though the molybdenum spectrum may be more monoenergetic due to the two characteristic x-ray peaks, because they are at lower energies (more near the K-edge), when the spectra are detected by the a-Se detector, the PHS and Swank are degraded.

IV. DISCUSSION

The model that we utilize in this work consists of a physics-based, Monte Carlo model to simulate the PHS as a function of incident-photon energy and applied electric field. It incorporates the effects of recombination and trapping in electron-hole pair transport.

For the simulation of electron-hole pairs, the current implementation samples the number of carriers generated with the corresponding burst size and thermalization distances. The subsequent transport takes into account the electron-hole pairs created, one burst at a time. When the secondary electron energy is high, the mean free path is larger in comparison to the burst and thermalization distances. However, when the secondary electron slows down, its range is reduced, and energy deposition events could happen closer together, potentially causing bursts to overlap with each other. Ideally, all bursts should be simulated at the same time to include overlapping effects in burst creation process and transport. However, since the run time increases with the number of carriers simulated simultaneously, a simpler implementation may be to simulate multiple bursts taking into consideration the distances between energy deposition events, where bursts created in close proximity can be simulated together to improve the physical accuracy of the model.

Recombination of electron-hole pairs leads to significantly fewer detected carriers, especially with low external electric field. In our work, recombination is considered to occur when a hole and an electron are within 1 nm of each other, where Coulombic attraction is assumed to be so strong that they cannot escape. However, since there are many

TABLE II. Simulated Swank factor for Mo/Mo (RQA-M 2) and W/Al standard radiation qualities with varying transport conditions.

Radiation quality (IEC 61267)	4 V/μm	30 V/Ltm	EHP creation
Mo/Mo (RQA-M 2)	0.878	0.922	0.929
W/Al	0.903	0.937	0.945

electron-hole pairs moving in the burst, several carriers can be found within the recombination radius at one time. In the current implementation, a first-hit search method was used. For each free carrier, the first carrier found to be in the recombination radius is chosen to be the carrier to be recombined. However, an exhaustive method can be used to search for the nearest neighbor for recombination. In principle, this nearest neighbor method is physically more accurate. In previous work,[28] we have reported that the mean recombination probability for the first-hit and the nearest neighbor techniques are the same in point bursts but differs in variance. The nearest neighbor method is also much more time consuming compared to the first-hit model and may require parallelization and additional speed up in order to be feasible in full x-ray signal formation simulations. The recombination probabilities using the nearest neighbor and first-hit methods need to be studied in more detail.

Trapping has a significant effect on electron-hole pair transport, especially in low applied electric field conditions where the carrier mobility is low. The current implementation considers only deep trapping of carriers with a constant carrier lifetime. When carriers are trapped, they are considered lost. More complex trapping models can be added in the future considering shallow traps, carrier releasing from traps, and trap filling effects.

Detector thickness is an important parameter to be considered for detailed transport simulation of electron-hole pairs and for DQE calculations. We show results for a detector thickness of 150 μm. For transport simulations, carrier transit time in the semiconductor material is directly proportional to its thickness. As the carrier transit time increases, the probability of the carrier getting trapped increases as well, thus affecting the PHS. Additionally, since the attenuation of the primary x-ray beam is a function of thickness, the DQE calculations are also affected. Therefore, the PHS and Swank for detectors with a range of thickness should be further studied.

V. CONCLUSION

Monte Carlo modeling of semiconductor detectors can provide insight into the fundamental physics and limitations of imaging systems. We report the use of novel three-dimensional spatiotemporal MC methods for simulation of PHS responses in a-Se detector including the effects of electron-hole pair transport. The simulated PHS were used for the study of Swank factors. Using monoenergetic x-rays between 10 and 140 keV, we show the Swank factor and DQE at zero spatial frequency as a function of incident-photon energy and transport conditions of the electron-hole pairs. Comparisons between simulated and experimental Swank factor using Gaussian fitting to have a good agreement of approximately 2% difference. The Swank factor computed using the full equation [Eqs. (10) and (12)] was found to be different than the Swank factor computed using the Gaussian approximation. The PHS using two mammography standard radiation qualities have been simulated with different electron-hole pair transport conditions, and Swank factors are calculated for different transport conditions. In order to provide further validation of the model, we are currently exploring experimental methods for PHS measurements for a-Se detectors.

a)Author to whom correspondence should be addressed. Electronic mail: yuan.fang@fda.hhs.gov

[1]G. Knoll, *Radiation Detection and Measurement* (Wiley Interscience/John Wiley and Sons, Inc., New Jersey, 2010), pp. 365–366.

[2]R. Schulz-Wendtland, K. Hermann, E. Wenkel, B. Adamietz, M. Lell, K. Anders, and M. Uder, "First experiments for the detection of simulated mammographic lesions: Digital full field mammography with a new detector with a double plate of pure selenium," Radiologe **51**, 130–134 (2011).

[3]E. Fourkal, M. Lachaine, and B. Fallone, "A comparison of x-ray detectors for mouse CT imaging," Phys. Med. Biol. **49**, 5251–5265 (2004).

[4]M. Bissonnette, M. Hansroul, E. Masson, and S. Savard, "Digital breast tomosynthesis using an amorphous selenium flat panel detector," Proc. SPIE **5745**, 529–540 (2005).

[5]E. Fredenberg, M. Hemmendorff, B. Cederström, M. Åslund, and M. Danielsson, Med. Phys. **37**, 2017–2029 (2010).

[6]A. Ginzburg and C. Dick, "Image information transfer properties of x-ray intensifying screens in the energy range from 17 to 320 keV," Med. Phys. **20**, 1013–1021 (1993).

[7]I. Blevis, D. Hunt, and J. Rowlands, "X-ray imaging using amorphous selenium: Determination of Swank factor by pulse height spectroscopy," Med. Phys. **25**, 638–641 (1998).

[8]I. Blevis, D. Hunt, and J. Rowland, "Measurement of x-ray photogeneration in amorphous selenium," J. Appl. Phys. **85**, 7958–7962 (1999).

[9]A. Badano and J. Sempau, "MANTIS: Combined x-ray, electron and optical Monte Carlo simulation of indirect radiation imaging system," Phys. Med. Biol. **51**, 1545–1561 (2006).

[10]A. Badano, I. Kyprianou, and J. Sempau, "Anisotropic imaging performance in indirect x-ray imaging detectors," Med. Phys. **33**, 2698–2713 (2006).

[11]F. Salvat, J. Fernandez-Varea, and J. Sempau, "PENELOPE-2006: A code system for Monte Carlo simulation of electron and photon transport," NEA No. 6222 (2006).

[12]I. Kawrakow and D. Rogers, "The EGSnrc code system: Monte Carlo simulation of electron and photon transport," Technical Report No. PIRS-701 (2001).

[13]MCNP—A General Monte Carlo N-Particle Transport Code, version 5, Technical Report No. LAUR-03-1987 (X-5 Monte Carlo team, 2003).

[14]S. Agostinelli *et al.*, "Geant4—A simulation toolkit," Nucl. Instrum. Methods Phys. Res. A **506**, 250–303 (2003).

[15]A. Ferrari, P. Sala, A. Fassuo, and J. Ranft, "FLUKA: A multi-particle transport code (Program version 2005)," Technical Report Nos. CERN-2005-10, INFN/TC-05/11, SLAC-R-773 (2005).

[16] A. Badal *et al.*, "penMesh-Monte Carlo radiation transport simulation in a triangle mesh geometry," IEEE Trans. Med. Imaging **28**, 1894–1901 (2009).

[17] M. Yunus, M. Kabir, and S. Kasap, "Sensitivity reduction mechanisms in amorphous selenium photoconductive x-ray image detectors," Appl. Phys. Lett. **85**, 6430–6432 (2004).

[18] K. Koughia, Z. Shakoor, S. Kasap, and J. Marshall, "Density of localized electronic states in a-Se from electron time-of-flight photocurrent measurement," J. Appl. Phys. **97**, 033706 (2005).

[19] E. Fourkal, M. Lachaine, and B. Fallone, "Signal formation in amorphous-Se-based x-ray detectors," Phys. Rev. B. **63**, 195–204 (2001).

[20] H. Barrett, J. Eskin, and H. Barber, "Charge transport in arrays of semiconductor gamma-ray detectors," Phys. Rev. Lett. **75**, 156–159 (1995).

[21] SYNOPSYS TCAD version Y-2006.06, Taurus Medici user guide (2006).

[22] SYNOPSYS TCAD, Sentaurus Device: Versatile, multifunctional device simulator, datasheet (2007).

[23] COMSOL, COMSOL Multiphysics 4.2a release notes (2011).

[24] S. Babiker, A. Asenov, J. R. Barker, and S. P. Beaumont, "Finite element Monte Carlo simulation of recess gate compound FFTs," Solid-State Electron. **39**, 629–635 (1995).

[25] T. Hayashi, Y. Kashio, and E. Okada, "Hybrid Monte Carlo-diffusion method for light propagation in tissue with a low-scattering region," Appl. Opt. **42**, 2888–2896 (2003).

[26] W. Que and J. Rowlands, "X-ray photogeneration in amorphous selenium: Geminate versus columnar recombination," Phys. Rev. B **51**, 10500–10507 (1995).

[27] J. Knight and E. Davis, "Photogeneration of charge carrier in amorphous selenium," J. Phys. Chem. Solids **35**, 543–554 (1975).

[28] D. Sharma, Y. Fang, F. Zafar, K. S. Karim, and A. Badano, "Recombination models for spatio-temporal Monte Carlo transport of interacting carriers in semiconductors," Appl. Phys. Lett. **98**, 242111 (2011).

[29] N. Bohr, "The penetration of atomic particles through matter," K. Dan. Vidensk. Selsk. Mat. Fys. Medd. **18**, 8 (1948).

[30] Y. Fang, A. Badal, N. Allec, K. S. Karim, and A. Badano, "Monte Carlo simulation of amorphous selenium imaging detectors," Proc. SPIE **7622**, 762214 (2010).

[31] W. M. Bartczak, M. P. DeHaas, and A. Hummel, "Computer simulation of the recombination of the ions in tracks of high-energy electrons in nonpolar liquids," Radiat. Phys. Chem. **37**, 401–406 (1991).

[32] H. Barrett and K. Myers, "Foundation of Imaging Science" (Wiley Interscience/John Wiley and Sons, Inc., New Jersey, 2004), pp. 748–763.

[33] R. K. Swank, "Absorption and noise in x-ray phosphors," J. Appl. Phys. **44**, 4199–4203 (1973).

[34] J. M. Boone, T. R. Fewell, and R. J. Jennings, "Molybdenum, rhodium, and tungsten anode spectral models using interpolating polynomials with application to mammography," Med. Phys. **24**, 1863–1874 (1997).